



Diverse rupture processes of the 2014 Kangding, China, earthquake doublet (M_W 6.0 and 5.7) and driving mechanisms of aftershocks

Xu Zhang^{a,b,*}, Wanpeng Feng^{c,d}, Dahu Li^e, Fengling Yin^a, Lei Yi^{f,g}

^a Institute of Geophysics, China Earthquake Administration, Beijing, China

^b Key Laboratory of Earthquake Source Physics, China Earthquake Administration, Beijing, China

^c Guangdong Provincial Key Laboratory of Geodynamics and Geohazards, School of Earth Sciences and Engineering, Sun Yat-Sen University, Zhuhai, China

^d Southern Marine Science and Engineering Guangdong Laboratory (Zhuhai), Zhuhai, China

^e Earthquake Administration of Sichuan Province, Chengdu, China

^f Key Laboratory of Comprehensive and Highly Efficient Utilization of Salt Lake Resources, Qinghai Institute of Salt Lakes, Chinese Academy of Sciences, Xining, China

^g Qinghai Provincial Key Laboratory of Geology and Environment of Salt Lakes, Qinghai Institute of Salt Lakes, Chinese Academy of Sciences, Xining, China

ARTICLE INFO

Keywords:

The 2014 Kangding earthquake doublet
Rupture complexity
Stress triggering
Driving mechanisms of aftershocks

ABSTRACT

An unusual earthquake doublet ruptured the high-risk middle segment of the Xianshuihe fault in November 2014, exhibiting significant variations in the rupture and aftershock characteristics. By conducting rupture kinematic inversions jointly with local broadband seismic data, strong-motion data, and coseismic InSAR data, we find diverse rupture processes of this earthquake doublet. The first event ruptured upward along the dip and bilaterally along the strike with the duration of 8.0 s, whereas the second event ruptured mainly around the hypocenter with the duration of 3.5 s. The estimated moment magnitudes of the first and second events of this earthquake doublet were M_W 6.0 and M_W 5.7, respectively. The further analysis of rupture model-based static and dynamic stress change suggests that the first event is likely responsible for triggering the second event. Based on the comprehensive analysis of aftershock migration features, we find complex and diverse driving mechanisms of aftershocks. Aftershocks of the first event of the earthquake doublet were likely driven by afterslip. Early aftershocks of the second event were also likely driven by afterslip; however, later aftershocks were likely driven by fluid diffusion. The revealed diverse rupture characteristics of the 2014 Kangding earthquake doublet sequence suggest the inherent strength and/or stress heterogeneities on the seismogenic faults.

1. Introduction

On 22 November 2014, a M_S 6.3 earthquake struck Kangding, a county in Sichuan Province, China. About three days later, another M_S 5.8 earthquake occurred approximately 10 km southeast of the epicenter of the M_S 6.3 earthquake (Fig. 1). The earthquake relocation results indicate that the hypocenter of the M_S 6.3 event was located at 30.2820°N, 101.6733°E, with a depth of 15.0 km, and the hypocenter of the M_S 5.8 event was located at 30.2031°N, 101.7151°E, with a depth of 13.6 km (Fang et al., 2015). The moment tensor solutions resolved with regional seismic waveforms indicate the nearly pure sinistral strike-slip mechanisms for both the M_S 6.3 and 5.8 events (Yi et al., 2015). In particular, the moment tensor solution for the M_S 6.3 event had a moment magnitude M_W 6.0, and a best double-couple faulting plane geometry with strike 143°, dip 82°, and rake -9°, and the moment

tensor solution for the M_S 5.8 event had a moment magnitude M_W 5.6, and a best double-couple faulting plane geometry with strike 151°, dip 83°, and rake -6°. For a typical mainshock-aftershock sequence, the Båth's law indicates that the minimum difference in magnitude between the mainshock and its largest aftershock is larger than 0.5 units (Shcherbakov and Turcotte, 2004). Moreover, due to the small spatial distance and elapsed time as well as the similar focal mechanisms between the M_S 6.3 and 5.8 events, hereafter we treat the two events as the 2014 Kangding earthquake doublet (Donner et al., 2015). The spatio-temporal distributions of the respective aftershocks of the first and second events highlight complex patterns with significant discrepancies, implying likely complex and diverse rupture processes of the 2014 Kangding earthquake doublet (Fig. 2).

The 2014 Kangding earthquake doublet occurred on the middle segment of the Xianshuihe fault. The 350-km-length sinistral strike-slip

* Corresponding author at: Institute of Geophysics, China Earthquake Administration, Beijing, China.

E-mail address: x.zhang@cea-igp.ac.cn (X. Zhang).

<https://doi.org/10.1016/j.tecto.2021.229118>

Received 12 April 2021; Received in revised form 6 October 2021; Accepted 17 October 2021

Available online 23 October 2021

0040-1951/© 2021 Elsevier B.V. All rights reserved.

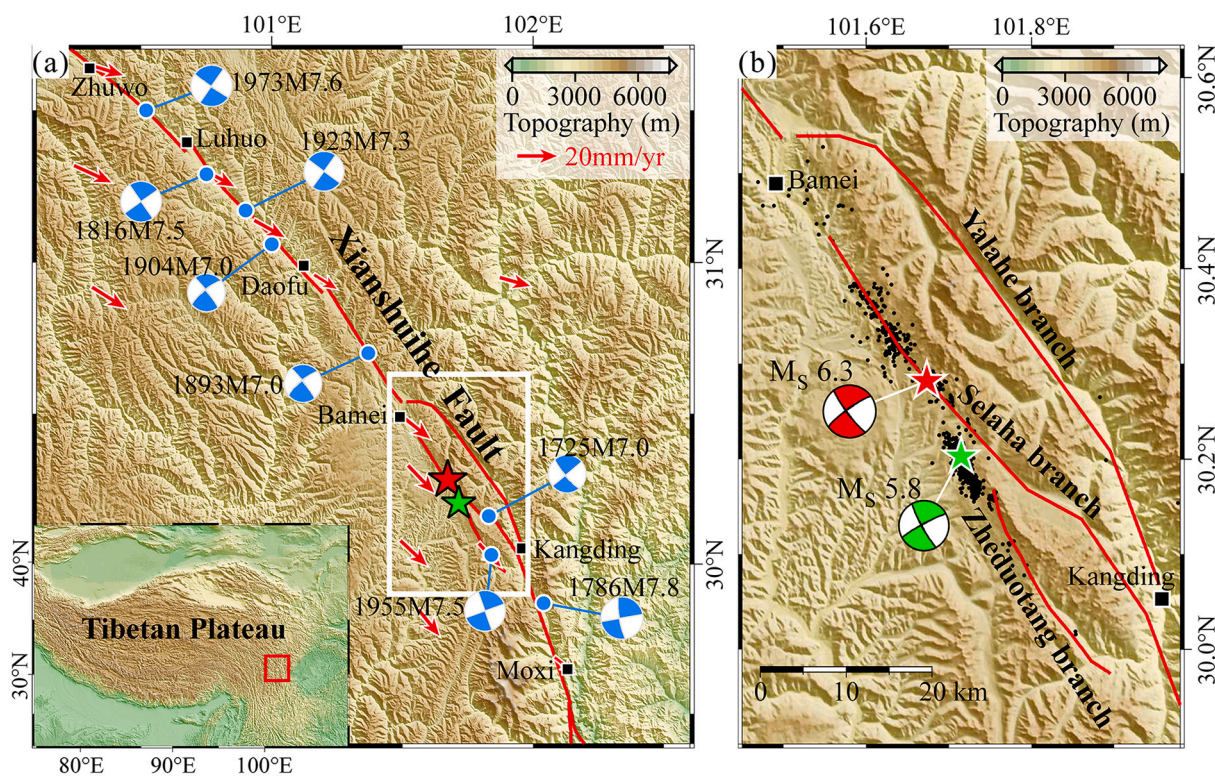


Fig. 1. (a) Background information on the regional tectonics and historical large earthquakes of $M \geq 7$. The red lines indicate the Xianshuihe fault (Wen et al., 2008; Yi et al., 2015). The blue dots and beach balls indicate the epicenter locations and focal mechanisms of the historical large earthquakes, respectively (Shan et al., 2013). The red arrows indicate GPS velocities relative to the stable Eurasia plate (Gan et al., 2007). The red rectangle in the bottom left inset indicates the region shown in the subplot (a), and the white rectangle indicates the region shown in the subplot (b). (b) Map view of seismicity (black dots) of the 2014 Kangding earthquake doublet sequence and focal mechanisms (red and green beach balls) of the two mainshocks. The locations of the relocated 2014 Kangding earthquake doublet sequence are from Fang et al. (2015). The red and green stars in both subplots (a) and (b) indicate the epicenter locations of the two mainshocks. (For interpretation of the references to colour in this figure legend, the reader is referred to the web version of this article.)

Xianshuihe fault is one of the most active intracontinental strike-slip fault systems in the world, on which the Holocene slip rate decreases from 15 mm/yr in the northwestern section to 5 mm/yr in the southeastern section, and has generated at least eight large earthquakes of $M \geq 7.0$ in the past 300 years (Allen et al., 1991; Wen et al., 2008). The latest large earthquake that struck this fault was the 1955 $M7.5$ earthquake, which was located nearby the source region of the 2014 Kangding earthquake doublet (Fig. 1a). Between Bamei and Kangding, the middle segment of the Xianshuihe fault bifurcates into the northern Yalaha branch, the middle Selaha branch, and the southern Zheduotang branch (Fig. 1; Allen et al., 1991; Yi et al., 2015). The first event of the earthquake doublet occurred on the Selaha branch, while the second event occurred on a previously unmapped fault between the Selaha and Zheduotang branches, which is likely the northwestern extension of the Zheduotang branch (Yi et al., 2015). Previous studies on the seismic hazard of the Xianshuihe fault, including rupture patterns of historical earthquakes (Allen et al., 1991; Wen et al., 2008), potential seismic gaps identified through the b -value distribution (Yi et al., 2008) and inter-seismic coupling model (Jiang et al., 2015b), and Coulomb stress evolution (Shan et al., 2013), consistently indicated that the northern segment of the Selaha branch is of high risk for a $M7+$ earthquake and close to rupture. However, the 2014 Kangding earthquake doublet may be not the anticipatory characteristic earthquake.

The 2014 Kangding earthquake doublet broke more than a 30-year quiet period without $M \geq 6$ earthquakes for the Xianshuihe fault, and it was unusual that the magnitude difference of the two largest earthquakes in an earthquake sequence within such short elapsed time is no more than 0.5 units if compared with the historical records of $M \geq 6$ earthquake sequences occurred on the Xianshuihe fault (Yi et al., 2015). The occurrence of the 2014 Kangding earthquake doublet sequence can

help better understand the likely segmentation feature of the Xianshuihe fault, which controls the nucleation and arrest of the earthquake (Allen et al., 1991). Besides, its occurrence can also help assess the regional seismic hazard of the Xianshuihe fault, especially for the high-risk northern segment of the Selaha branch (Shan et al., 2013; Wen et al., 2008).

Jiang et al. (2015a) have used one Interferometric Synthetic Aperture Radar (InSAR) interferogram to invert static slip models of the 2014 Kangding earthquake doublet and found that the coseismic deformation was mainly caused by the rupture of the first event. In this study, we first image the rupture processes of this earthquake doublet with local seismic and InSAR data. Based on the combined analysis of the rupture model-based static and dynamic stress change, we discuss whether the first event of this earthquake doublet is responsible for triggering the second event. Afterward, we further investigate the driving mechanisms of aftershocks of the 2014 Kangding earthquake doublet.

2. Data and method

Previous studies have indicated that comprehending the earthquake rupture process is significant to enhance our understanding of the earthquake rupture physics and the relationship between the earthquake rupture and seismogenic environment and to assess the potential seismic hazard (e.g., Avouac et al., 2015; Hartzell et al., 2013; Yue et al., 2017; Zhang et al., 2020b). The available abundant local seismic and InSAR data provide us a unique opportunity by combining them to image the rupture processes of the 2014 Kangding earthquake doublet with high spatial and temporal resolutions. In this study, we collected the local seismic data from seven broadband seismic stations and six strong-motion stations and the coseismic InSAR Line-of-Sight (LOS)

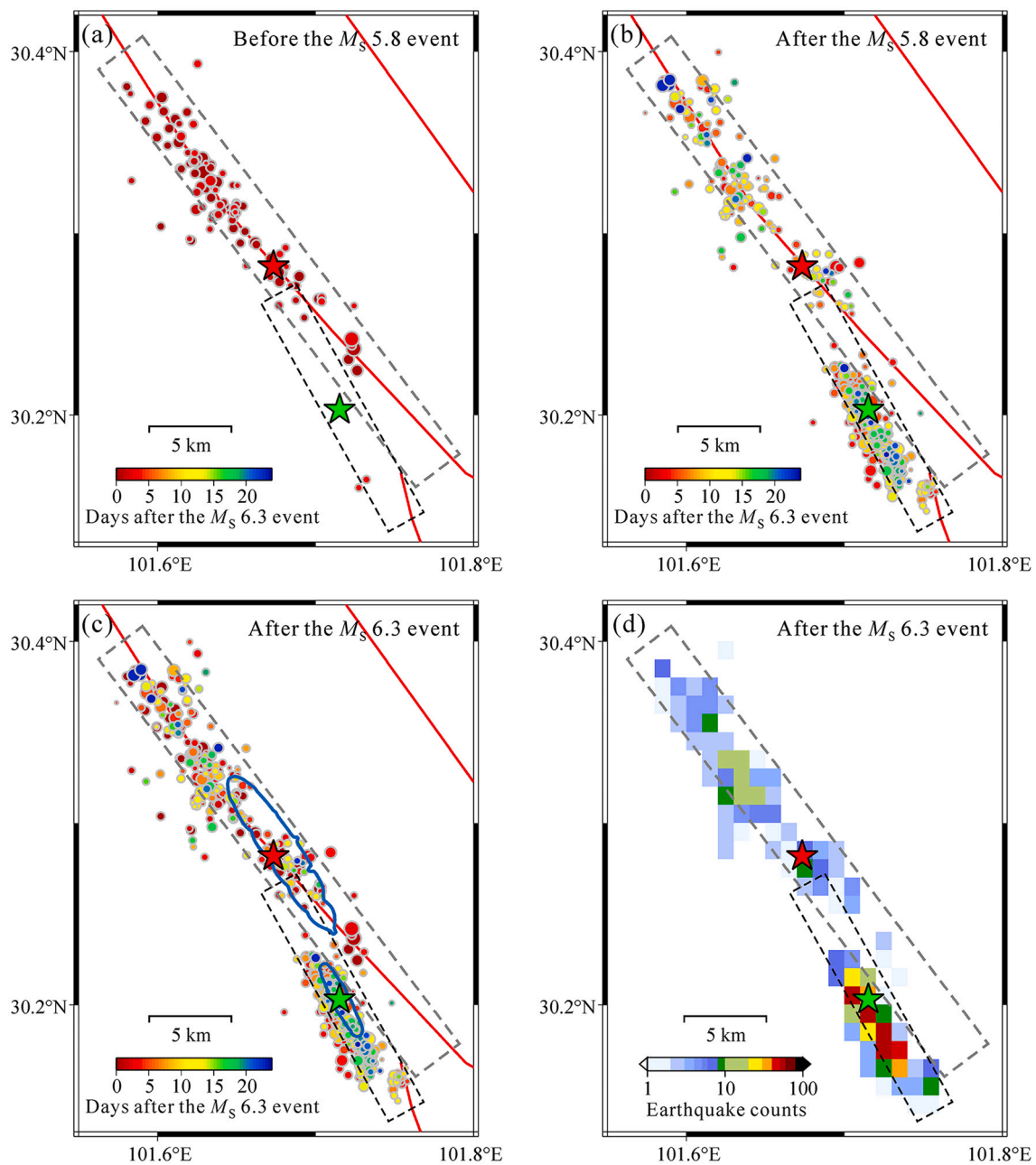


Fig. 2. Spatiotemporal evolution of seismicity. (a) Distribution of the aftershocks (colour-coded circles) before the second event of the earthquake doublet. (b) Distribution of the aftershocks after the second event. (c) Distributions of all aftershocks and the inferred main slip patches of this earthquake doublet which are depicted by blue 0.1-m coseismic slip contours. (d) Distribution of cumulative earthquake counts in each divided cell of $0.02^\circ \times 0.02^\circ$. The red and green stars in each panel indicate the epicenter locations of the first and second events of the earthquake doublet, respectively. The dashed gray and black rectangles in each panel indicate the initial planar fault models for inverting the rupture processes of the first and second events, respectively. The red lines in panels (a)–(c) indicate the branches of the Xianshuihe fault. (For interpretation of the references to colour in this figure legend, the reader is referred to the web version of this article.)

displacement data to investigate the rupture processes of the 2014 Kangding earthquake doublet in detail.

2.1. Local seismic data

The local seismic data were collected from seven three-component broadband seismic stations (BAX, DFU, GZA, JLO, LTA, XJI, and YJI) and six three-component strong-motion stations (51BXY, 51DFB, 51HYY, 51KDL, 51SMX, and 51YAL) with epicentral distances less than 150 km (Fig. 3). Note that the strong-motion station 51KDL was deployed after the first event of this earthquake doublet and hence had no recordings of this event. In addition, the station 51DFB also had no

recordings of the first event. For the second event of this earthquake doublet, only the station 51BXY had no recordings. The velocity waveforms from the broadband seismic stations were band-pass filtered with a frequency band of 0.05–0.25 Hz to reduce the local site effects (Graizer, 2006; Wang et al., 2013). The unfiltered three-component waveforms recorded by the nearest broadband station GZA are shown in Fig. S1. The acceleration recordings from the strong-motion stations were first integrated into velocity waveforms and then filtered with the same frequency band of 0.05–0.25 Hz. The orthonormalization method (Wang, 1999) and the local 1-D velocity model (Fig. S2; Yi et al., 2015) were utilized to compute the corresponding Green's functions. Moreover, the synthetic data were filtered in the same frequency band as the

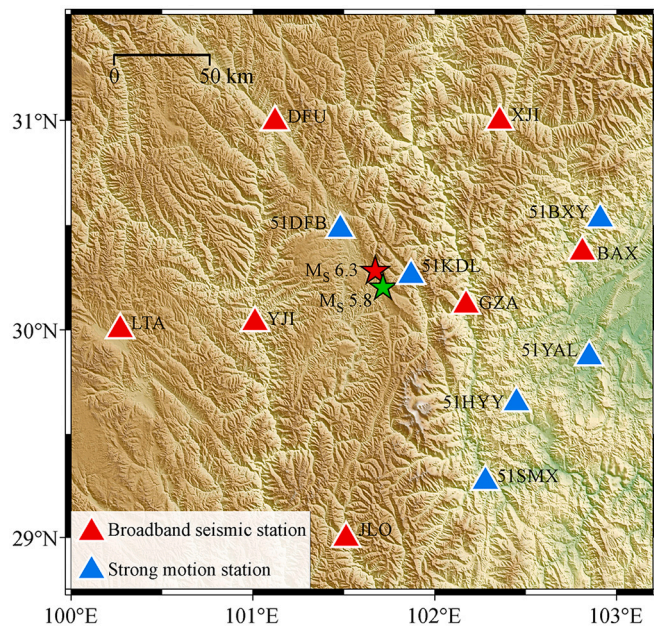


Fig. 3. Distribution of the broadband seismic stations (red triangles) and strong-motion stations (blue triangles) used in this study. (For interpretation of the references to colour in this figure legend, the reader is referred to the web version of this article.)

observation data.

2.2. Coseismic InSAR data

The coseismic InSAR LOS displacement data were from an L-band ALOS-2 interferogram of 20140926–20150925 in track T147 and a C-band Sentinel-1 interferogram of 20141112–20141206 in track T26. The observations were obtained by using an automated InSAR processing chain, based on the open-source InSAR software package, GMTSAR (Feng et al., 2016; Sandwell et al., 2011). The 30-m Shuttle Radar Topography Mission (SRTM) digital elevation model (DEM) data were applied during the InSAR processing (Farr et al., 2007). To reduce the effects of strong atmospheric effects (APS) in the region, we used the DEM data to estimate a best fitting plane with a three-parameter polynomial by considering the linear correlation between the APS and local topography (Feng et al., 2013). To reduce the effects of spatially correlated noise and the computational burden in the finite-fault inversion, we down-sampled the two interferograms into 8018 and 4900 points, respectively, by using a quadtree algorithm (Simons et al., 2002). The obtained InSAR deformation patterns suggest that the main coseismic surface deformation was induced by the first event of this earthquake doublet (Fig. S3). We used the codes EDGRN/EDCMP developed by Wang et al. (2003) and the same 1-D velocity model described above to compute the corresponding Green's functions.

2.3. Inversion method and model parameterization

Based on the distribution of aftershocks and the coseismic deformation area, we fixed the geometric planar fault models of the 2014 Kangding earthquake doublet. The planar fault of the first event is 32 km long along the strike direction (strike = 143°) and 24 km wide along the down-dip direction (dip = 82°) from the ground surface and is gridded into 192 sub-faults of 2 km × 2 km. Moreover, the planar fault of the second event is 16 km long along the strike direction (strike = 151°) and 20 km wide along the down-dip direction (dip = 83°) and is gridded into 80 sub-faults of 2 km × 2 km. Following the finite-fault inversion method applied in the previous studies (Zhang et al., 2020a; Zhang et al.,

2012), we inverted the rupture processes of the first event jointly with the local seismic and coseismic InSAR data and the second event with the local seismic data. This inversion method does not need a priori constraint for the shape of each sub-fault slip function, which is instead determined through an iterative process utilizing the conjugate gradient method (Ward and Barrientos, 1986). Moreover, this inversion method allows arrival time shifts to align the waveform data in the finite-fault inversion. The kinematic inversion of the earthquake rupture process needs a priori constraints of maximum rupture velocity and rise time for each sub-fault. In this study, with a given maximum rupture velocity of 3.0 km/s, corresponding to approximately 85% local S-wave velocity, the preferred maximum rise times for the first and second events are 5 s and 3 s, respectively (Fig. S4).

Determining the optimal weight values between different datasets is important in joint inversion. The overweighting of one dataset will result in poor explanations of the other datasets. In this study, we adopted a grid search strategy to obtain the optimal weight values of the local seismic and InSAR datasets used for joint inversion of the rupture process of the first event. As shown in Fig. S5, when the relative weight value of the InSAR dataset is equal to 3, the average misfit of the two datasets reaches the global minimum. The misfit is computed with the equation $misfit = \frac{\sum_i (d_i - s_i)^2}{\sum_i d_i^2}$, where d_i and s_i represent the observed and synthetic data, respectively. For the waveform data, the subscript i indicates an index over the stations, components, and times; however, for the InSAR data, the subscript i indicates an index over the observed points. Moreover, the normalization of the misfit for each data set means that the computed misfits are divided by their maximum value. Thus, the ultimately adopted optimal weight values of the local seismic and InSAR datasets are 1 and 3, respectively.

3. Results

The whole rupture process of the first event of the 2014 Kangding earthquake doublet released a scalar seismic moment of 1.46×10^{18} Nm, corresponding to a moment magnitude of M_W 6.0. The duration was no more than 10 s, with 90% moment released in the first about 8.0 s (Fig. 4a). The inverted slip pattern shows that the first event ruptured upward along dip and bilaterally along strike, having a peak slip of 0.50 m (Fig. 4b). The main rupture length and width are approximately 11 km and 12 km, respectively. Fig. 4c shows the detailed rupture time and source time function of each sub-fault. Comparison between the observations and model predictions are shown in Figs. 4d–4j. The predicted local seismic waveforms are in good agreement with the observations, with most of the arrival times and amplitudes being well reproduced (Fig. 4d). In particular, based on our model, the local seismic data are explained with a variance reduction (VR) of 64%. Moreover, our rupture model of the first event can well recover the observed major deformation pattern (Figs. 4e–4j), and the data fits between the predicted and observed displacements have a root-mean-square error of 0.75 cm.

We also used the same fault parameterization and modeling approach mentioned above to conduct finite-fault inversion of the first event with only InSAR data. Compared with our preferred rupture model from joint inversion, the only InSAR data-based rupture model shows a larger rupture area and more clear slip at shallow depth (Figs. S6 and 4b). The discrepancies may attribute to the improved stability and resolution of rupture model from the joint inversion of multi-source data as previous studies have suggested (e.g., Bletery et al., 2014; Cesca et al., 2017; Gusman et al., 2015; Yue et al., 2014; Zhang et al., 2012). Moreover, the relatively long observation interval of the used InSAR data may include some deformation sources of postseismic afterslip.

The whole rupture process of the second event released a scalar seismic moment of 3.93×10^{17} Nm, corresponding to a moment magnitude of M_W 5.7. The duration was no more than 5 s, with 90% moment released in the first about 3.5 s (Fig. 5a). The inverted slip pattern shows that the second event ruptured mainly around the initial

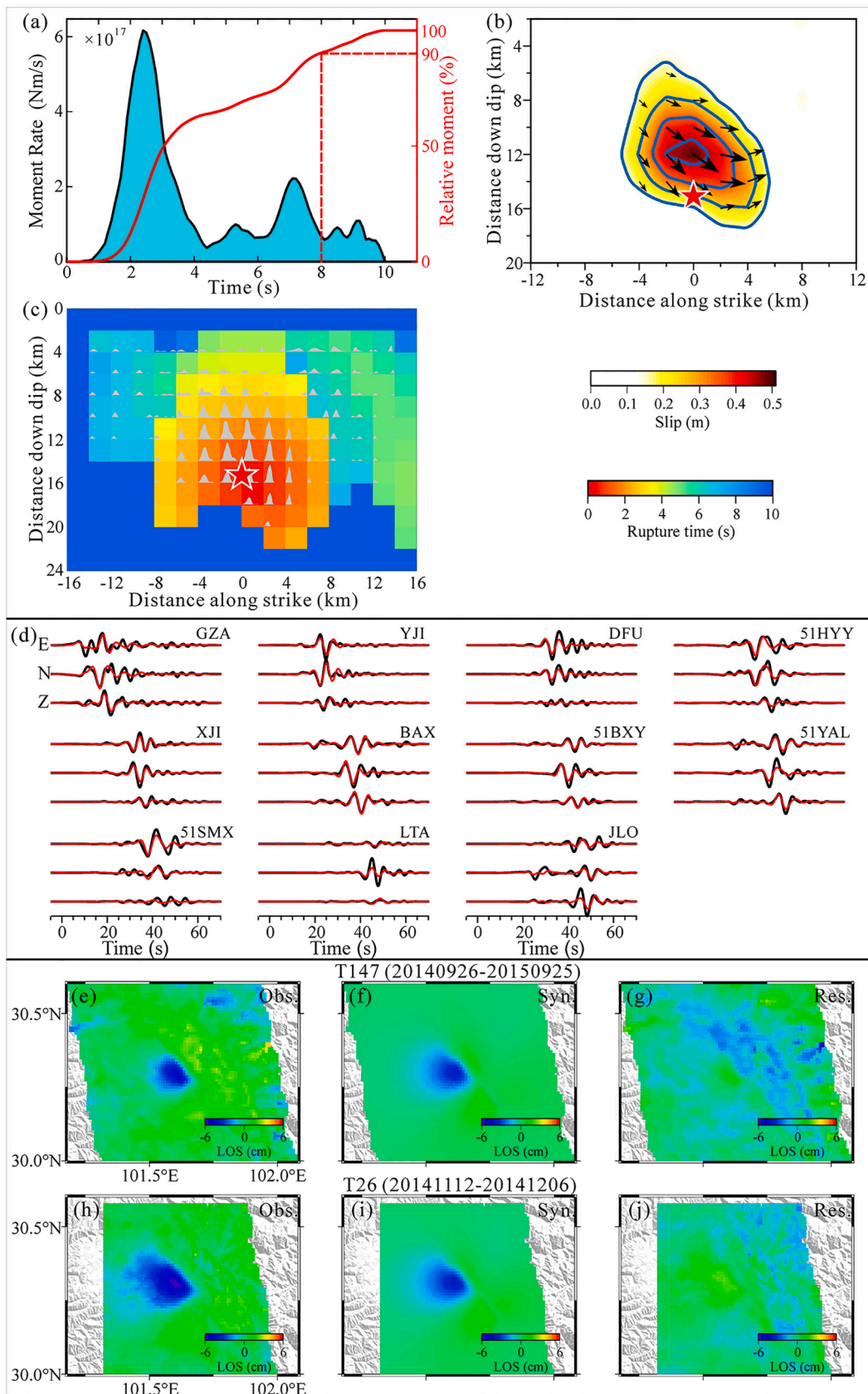


Fig. 4. The inverted rupture scenario of the first event and the data fitting. (a) Source time function. (b) Coseismic slip pattern. The blue lines indicate the slip contours of 0.15 m, 0.25 m, 0.35 m, and 0.45 m, respectively. The black arrows indicate slip directions and the red star indicates the initial rupture point. (c) Slip function (gray shaded region) and rupture time of each sub-fault. (d) Comparison of the observed local seismic data (black lines) and the synthetics (red lines). (e)-(g) Observed InSAR LOS displacements from track 147, synthetic data, and their residuals. (h)-(j) Same as (e)-(g) but for the InSAR data from track 26. (For interpretation of the references to colour in this figure legend, the reader is referred to the web version of this article.)

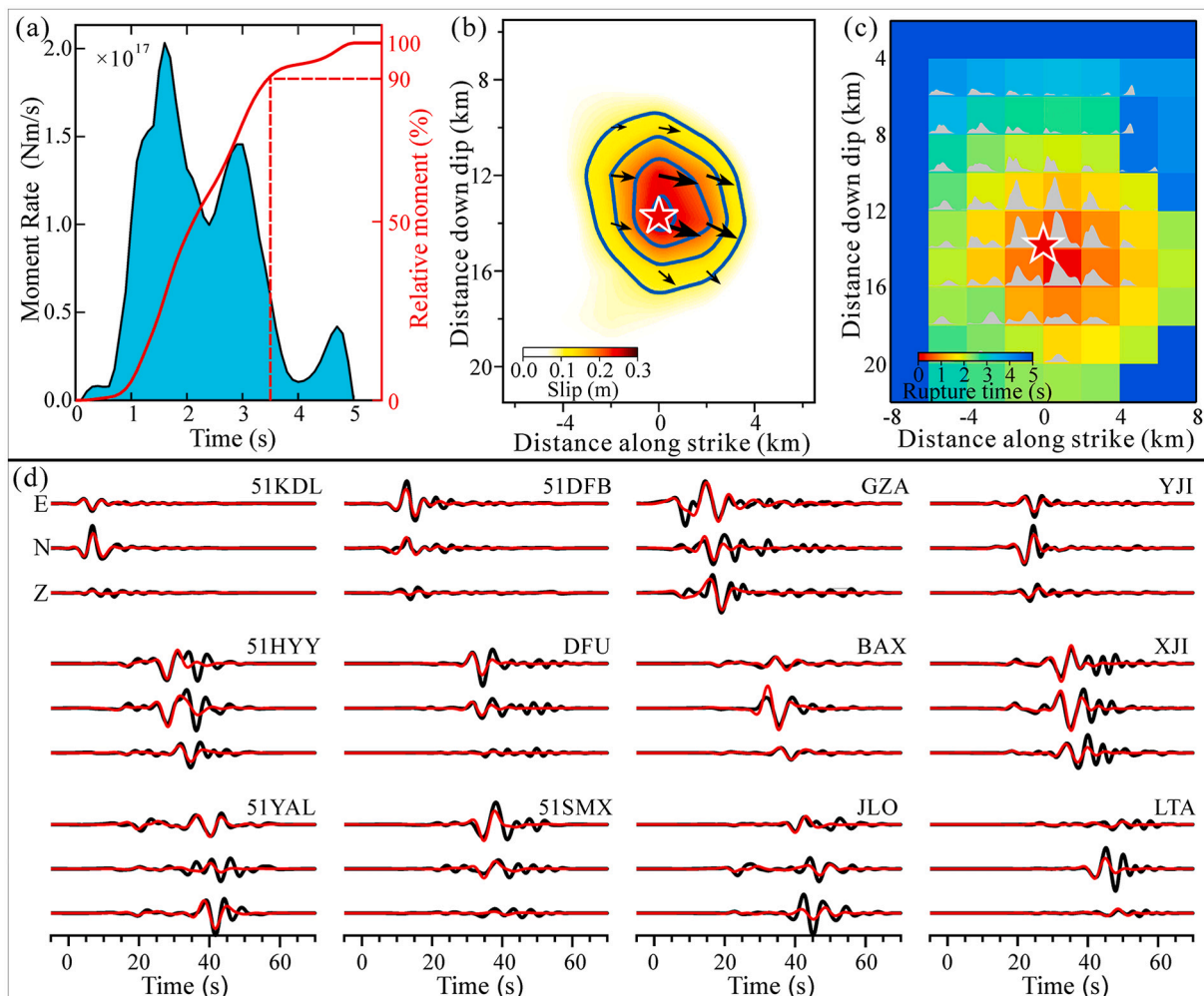


Fig. 5. Same as Fig. 4 but for the second event. Note: the blue lines in the subplot (b) indicate the slip contours of 0.10 m, 0.15 m, 0.20 m, and 0.25 m, respectively. (For interpretation of the references to colour in this figure legend, the reader is referred to the web version of this article.)

rupture point and had no significant rupture directivity (Fig. 5b). The peak slip obtained from the inverted rupture model is 0.28 m. The main rupture length and width are approximately 7 km and 8 km, respectively. Fig. 5c shows the detailed rupture time and source time function of each sub-fault. Based on our rupture model of the second event, the predicted local seismic waveforms are also in good agreement with the observations (Fig. 5d). Specifically, the local seismic data can be explained with a VR of 70%. Moreover, we modeled the LOS displacements at the same observation points of the InSAR data used in this study with the local seismic data-based rupture model of the second event (Fig. S7). Compared with the observations, the predicted LOS displacements are much small.

To further evaluate the reliability of the inversion results, we conducted jackknife tests following Chen et al. (2020) for the first and second events, respectively. We randomly removed 20% of each data set and repeated the inversion with the same inversion parameters 50 times to obtain the mean, standard deviation, and coefficient of variation (CV, the standard deviation divided by the mean of the slip). The jackknife test results highlight the reliability of the recovered slip patterns (Fig. 6).

Moreover, we tested the variation of hypocentral depth in affecting the inversion results. With the same inversion parameters, we artificially shifted hypocentral depth by ± 2 km and then repeated the finite-fault inversion. We find that the on-fault locations of the inverted slip patches depend on the hypocentral depths; however, the main features of the slip patterns are similar (Figs. S8, 4b, and 5b). It's noteworthy that the hypocenter locations of the earthquake doublet used in the finite-

fault inversions were relocated by Fang et al. (2015) with the double-difference algorithm (Waldhauser and Ellsworth, 2000) and the dense near-source and local seismic stations. As reported by Fang et al. (2015), the depth uncertainties of the relocated mainshocks were less than 0.2 km. The relatively fine relocation results can provide good constraints in determining the on-fault locations of the slip patches.

4. Discussion

4.1. Rupture characteristics of the 2014 Kangding earthquake doublet sequence and its implication

The mainshock-aftershock sequence is one of the fundamental characteristics in observational seismology, although the actual physical mechanism of aftershock generation is not well known. Some previous studies have found a strong spatial complementary pattern between mainshock rupture and aftershock distribution (e.g., Beroza and Zoback, 1993; Mendoza and Hartzell, 1988; Wetzler et al., 2018; Yue et al., 2017). To explore whether the 2014 Kangding earthquake doublet sequence has a similar pattern, we projected the aftershocks relocated by Fang et al. (2015) with the double-difference algorithm (Waldhauser and Ellsworth, 2000) onto the fixed planar faults of the 2014 Kangding earthquake doublet (Fig. 7). As reported by Fang et al. (2015), the horizontal uncertainties of the relocated aftershocks were less than approximately 0.2 km and the depth uncertainties were less than 0.3 km. Most of the aftershocks were located outside of and near the edge of the

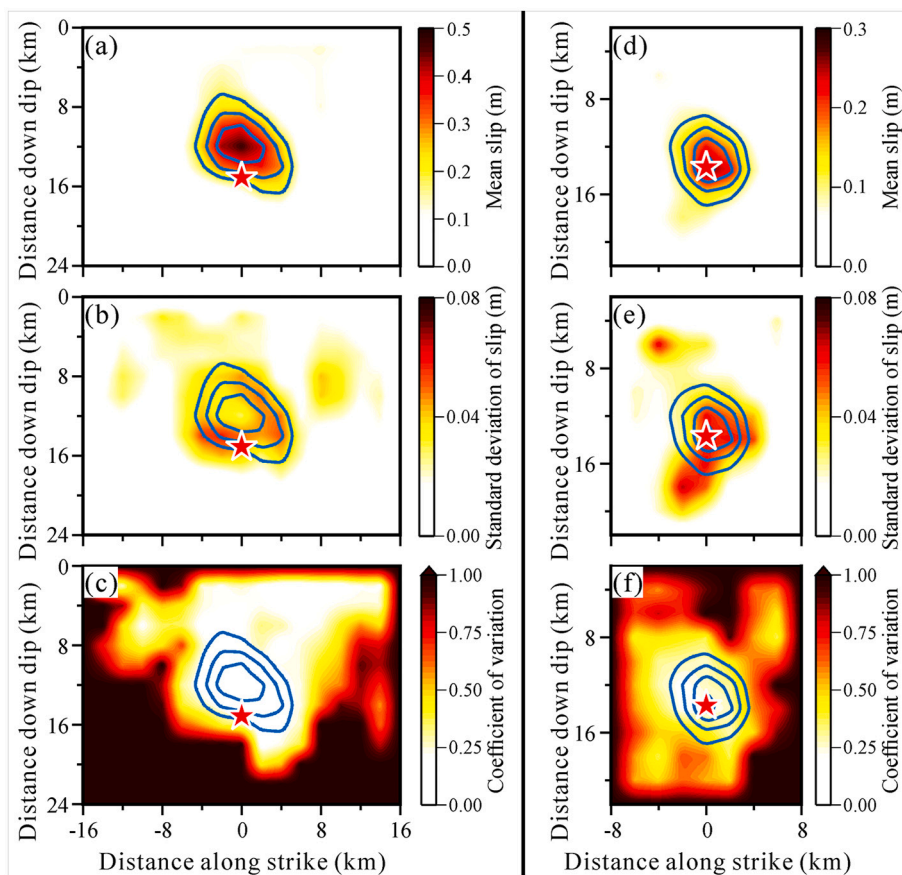


Fig. 6. Jackknife tests for the 2014 Kangding earthquake doublet. (a)-(c) Mean slip, standard deviation of slip, and the coefficient of variation CV for the first event. The blue lines indicate the slip contours of the preferred rupture model shown in Fig. 4b. (d)-(f) Same as (a)-(c) but for the second event. The blue lines indicate the slip contours of the preferred rupture model shown in Fig. 5b. (For interpretation of the references to colour in this figure legend, the reader is referred to the web version of this article.)

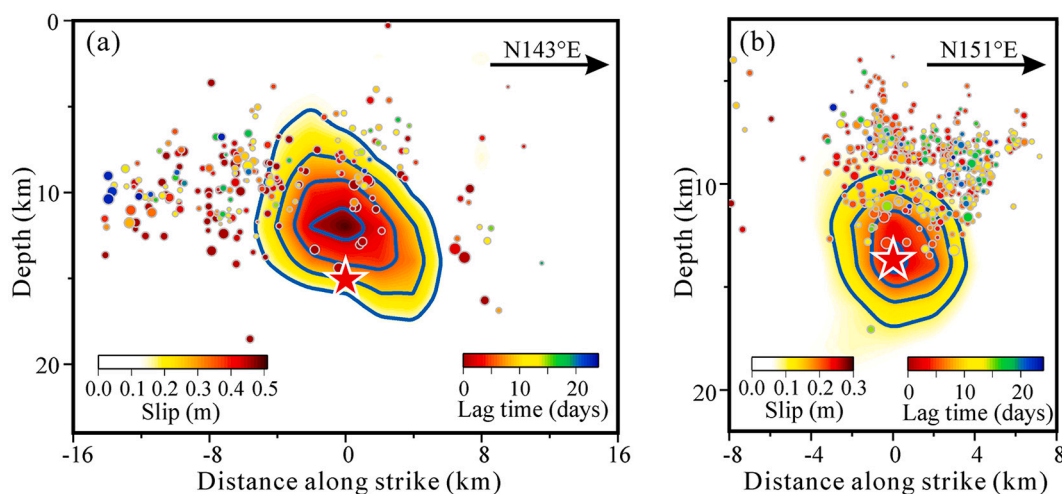


Fig. 7. Distributions of the aftershocks (colour-coded circles) and coseismic slip for the first event (a) and the second event (b).

regions with large coseismic slip. Moreover, we can observe that some aftershocks overlapped the mainshock rupture areas especially in the regions with large spatial gradients of the coseismic slip, but few aftershocks were located in the peak slip region. One potential mechanism for this feature was that the earthquake did not fully release the accumulated strain energy around the edge of the main rupture area. In addition, the remaining residual stress in the weak coseismic slip region with a large spatial gradient could also play an important role in promoting the occurrence of aftershocks (Beroza and Zoback, 1993; Wetzler et al., 2018; Yabe and Ide, 2018). Some previous studies have suggested

that afterslip is another important postseismic mechanism in controlling aftershock distribution (e.g., Feng et al., 2020; Perfettini et al., 2018). The rapid afterslip may play an important role in resulting in the interesting spatial complementary pattern between the aftershock distribution and coseismic rupture of the 2014 Kangding earthquake doublet. Moreover, based on the 2-D earthquake sequence simulations, Ozawa and Ando (2021) have proposed that the increase of local stress caused by rupture of the mainshock is also likely to trigger aftershocks on the nearby small subsidiary faults. Thus, it may explain the distribution of some scattered aftershocks (Fig. 2c). It is noteworthy that the

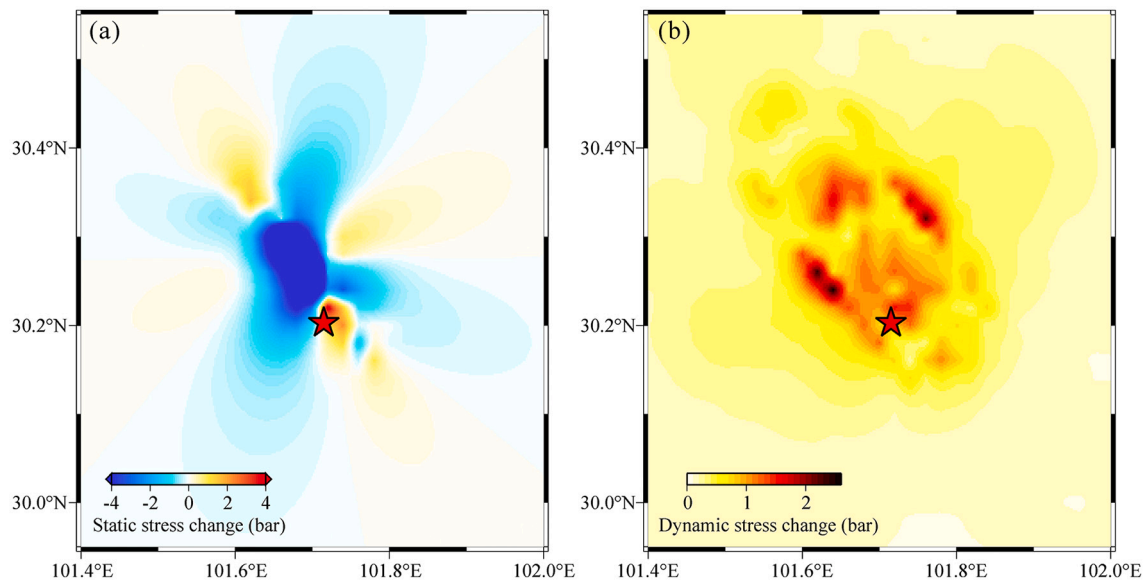


Fig. 8. Stress changes caused by the first event of the earthquake doublet. (a) Static stress change. (b) Dynamic stress change. The calculated static and dynamic stress changes are both at the focal depth of the second event. The red star in each subplot indicates the epicenter location of the second event. (For interpretation of the references to colour in this figure legend, the reader is referred to the web version of this article.)

spatial pattern between the aftershock distribution and the coseismic slip of the first event and the corresponding pattern of the second event have some individually discrepant features. Most aftershocks of the first event were distributed on the northwest of the main coseismic slip zone and had a similar depth range with the main ruptured asperity; nevertheless, a significant aftershock deficit zone existed on the southeast of the main coseismic slip zone (Figs. 7a and 2). However, most aftershocks of the second event were located out of and near the edge of the main ruptured asperity at shallower depths.

The moment magnitudes of the 2014 Kangding earthquake doublet estimated from the inversion results are smaller than the surface wave magnitude by 0.3 units. The discrepancies are likely from the reasons that the used seismic data and the calculating methods are different (Wells and Coppersmith, 1994). Surface wave magnitude is estimated from the seismic wave amplitudes at the approximately 20-s period recorded by different stations. The calculated surface wave magnitudes are likely affected by station azimuth, epicentral distance, and crustal structure. However, moment magnitude is a direct measurement of the released energy of an earthquake. Wells and Coppersmith (1994) have proposed that the moment magnitude is a more accurate measurement for an earthquake size than the traditional surface wave magnitude. Moreover, our rupture models highlight strong slip heterogeneities of the 2014 Kangding earthquake doublet (Figs. 4b and 5b). The first event nucleated at a relatively deep depth and ruptured mainly at the shallow depth, which exhibits significant up-dip rupture directivity. However, the main rupture of the second event concentrated almost around its initial rupture point. Considering the adopted maximum frequency of 0.25 Hz for the local seismic data, the only local seismic data-based inversion results of the second event may not well resolve the small-scale rupture features. Thus, we cannot rule out the possibility that the resolved nearly circular slip patch of the second event may be caused by the frequency limitation.

Distributions of the epicenter locations of aftershocks and the inferred main slip patches of this earthquake doublet show a potential seismic gap with slip deficit and few aftershocks (Fig. 2c). Moreover, our preferred rupture models show significant on-fault slip deficit zones (Figs. 4b and 5b). Two physical mechanisms are likely to interpret such features. One is that the slip deficit zones have high mechanical strength (Corbi et al., 2017; Das and Henry, 2003; Gallovič et al., 2020). The other one is that the slip deficit zones are creeping, thus lack of sufficient

accumulated strain energy to release during earthquake rupture (Harris, 2017; Kim et al., 2016). The previous geodetic study showed that the seismogenic faults of the 2014 Kangding earthquake doublet have large interseismic coupling ratios at depths shallower than 20 km, possessing the potential to host a M7+ earthquake (Jiang et al., 2015b). However, the cumulative seismic moment of this earthquake doublet was 1.85×10^{18} Nm, corresponding to a moment magnitude of M_w 6.1 which is much smaller than the magnitude of the anticipatory characteristic earthquake. Thus, we suggest that the middle segment of the Xianshuihe fault, on which the 2014 Kangding earthquake doublet occurred, still poses a large seismic risk; in addition, the revealed shallow slip deficit implies that the future large earthquake may overcome the fault strength at the subsurface and eventually rupture the surface (Gallovič et al., 2020).

4.2. Did the first event of the earthquake doublet trigger the second event?

Stress perturbations have been recognized as an important physical mechanism in understanding earthquake triggering. Previous studies have revealed that small static and/or dynamic stress changes (as low as 0.1 bar) from local and regional earthquakes can be able to trigger the occurrence of the subsequent earthquakes in the adjacent region (e.g., King et al., 1994; Wallace et al., 2017). To explore the potential triggering relationship of the 2014 Kangding earthquake doublet, we calculated the static and dynamic stress changes caused by the first event around the source region of the second event.

Based on our rupture model of the first event, we utilized the software PSGRN/PSCMP developed by Wang et al. (2006) to calculate the static Coulomb stress change on an interface fixed at the focal depth of the second event (Fig. 8a). Receiver fault parameters were from the focal mechanism of the second event. With a commonly used effective coefficient of friction of 0.4, the rupture of the first event increased the stress by 0.81 bar at the location of the hypocenter of the second event.

The peak dynamic stress change is related to the peak ground velocity (PGV) of the seismic waveform (Li et al., 2019; van der Elst and Brodsky, 2010). Based on the rupture model of the first event, we modeled the velocity waveforms on an interface fixed at the focal depth of the second event using the same orthonormalization method and local 1-D velocity model described above. The modeled velocity waveforms were filtered with the same frequency band of 0.05–0.25 Hz as used in

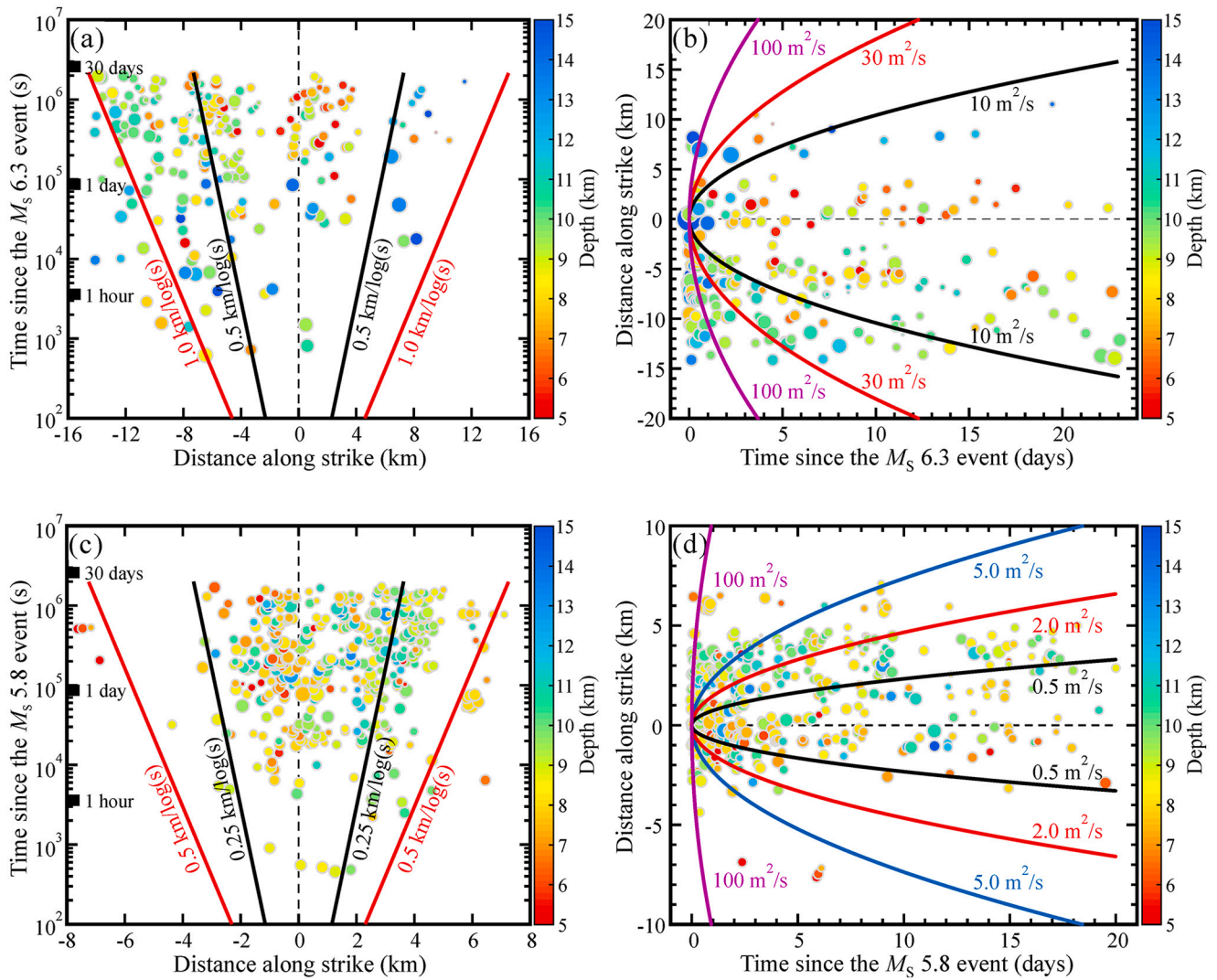


Fig. 9. Spatiotemporal evolution of aftershocks of the first event (a)-(b) and of the second event (c)-(d). Black and red lines in (a) and (c) show the migration with the logarithm of time. Colour lines in (b) and (d) highlight the predictions from the fluid diffusion model. (For interpretation of the references to colour in this figure legend, the reader is referred to the web version of this article.)

the above finite-fault inversion. Within the near-field distance which we are concerned in this study, the largest dynamic stress change should be from the passage of the S waves (Boatwright et al., 2001). Thus, based on the modeled velocity waveforms, we then followed Li et al. (2019) to estimate the peak dynamic stress with a 30-GPa shear modulus and 3.58-km/s local S -wave velocity of the source region. The estimated results show that the peak dynamic stress reaches 0.89 bar at the location of the hypocenter of the second event (Fig. 8b). Due to the lack of the relatively high-frequency components in the modeled velocity waveforms, the estimated peak dynamic stress should be considered as the lower boundary value.

The combined analysis of the static and dynamic stress changes strongly suggests that the rupture of the first event of the 2014 Kangding earthquake doublet had an important role in triggering the second event, and the transferred stress is likely to alter the properties of the seismogenic fault of the second event and to promote the fault failure.

4.3. Driving mechanisms of aftershocks

Aftershocks of the 2014 Kangding earthquake doublet exhibit complex migration features (Figs. 2 and 9). For aftershocks of the first event of the earthquake doublet, we can observe that the aftershock zone

shows a logarithmic expansion with time (Fig. 9a), which is well characterized by the migration pattern of aftershocks driven by the afterslip model (Perfettini et al., 2018). The migration speed of the aftershocks of the first event was estimated to be around $\sim 1.0 \text{ km}/\log(\text{s})$, which is also consistent with the observed migration speeds of aftershocks driven by afterslip from some previous studies (Fang et al., 2018; Warren-Smith et al., 2017). Another predominant driving mechanism of aftershocks is the fluid diffusion, of which the aftershocks migration front can be modeled with the relationship $r = \sqrt{4\pi Dt}$, where r is distance, D is diffusivity, and t is time (Shapiro et al., 1997). Diffusivity values as high as 10–30 m^2/s are required to match the migration pattern if aftershocks of the first event were driven by fluid diffusion (Fig. 9b). However, previous studies have found that the diffusivity values for fluid-driven earthquake sequences are commonly in the range of 0.2–2.0 m^2/s (Shapiro et al., 1997; Shelly et al., 2016; Shelly et al., 2013). Although some authors have pointed out the diffusivity value may be up to 6 m^2/s for some special earthquake sequence (Ross et al., 2017), the required diffusivity value of 10–30 m^2/s here is still unreasonably large (Koper et al., 2018; Warren-Smith et al., 2017). Thus, based on the above analysis, we prefer afterslip as the likely driving mechanism of aftershocks of the first event.

For aftershocks of the second event, the estimated general after-slip

migration speed was around ~ 0.50 km/log(s) (Fig. 9c), which is a little smaller than the migration speed of aftershocks of the first event. Afterward, we also applied the fluid-driven model in the aftershock sequence of the second event (Fig. 9d). Intriguingly, we can observe that aftershocks of the second event were driven by more complex mechanisms. Diffusivity values as high as $5\text{--}100$ m²/s are required to match the aftershock migration in the first ~ 3 days; however, diffusivity values of $2\text{--}5$ m²/s are relatively good to match the aftershock migration later on. Thus, we suggest that aftershocks of the second event were driven by both afterslip and fluid diffusion. Specifically, early aftershocks were likely driven by afterslip, and then the fluid diffusion process played the predominant role. Similar complex driving mechanisms of aftershocks have also been found in studying the 2010 M_W 7.2 El Mayor-Cucapah earthquake sequence by Ross et al. (2017).

5. Conclusions

Based on the local seismic and coseismic InSAR data, we investigated the rupture complexity of the 2014 Kangding earthquake doublet in detail. The finite-fault inversion results indicate the diverse rupture processes of the 2014 Kangding earthquake doublet. The first event of this earthquake doublet ruptured upward along the dip and bilaterally along the strike, and released a seismic moment of 1.46×10^{18} Nm, corresponding to a moment magnitude of M_W 6.0, with a duration of 8.0 s. The second event ruptured mainly around the hypocenter without significant rupture directivity, and released a seismic moment of 3.93×10^{17} Nm, corresponding to a moment magnitude of M_W 5.7, with a duration of 3.5 s. Moreover, distributions of aftershocks and coseismic slips of the first and second events show diverse spatial complementary patterns. Based on the combined analysis of static and dynamic stress change, we find that the rupture of the first event of the earthquake doublet had an important role in triggering the second event. Besides, the comprehensive analysis of aftershock migration features reveals complex driving mechanisms of aftershocks. Aftershocks of the first event migrated with the logarithm of time and were likely driven by afterslip. Early aftershocks of the second event had a similar migration feature with aftershocks of the first event; however, the migration of later aftershocks exhibited a distinct feature that can be well modeled by the fluid diffusion process. We suggest that the inherent strength and/or stress heterogeneities on the seismogenic faults are likely to result in the diverse rupture characteristics of the 2014 Kangding earthquake doublet sequence.

Declaration of Competing Interest

The authors declare that they have no known competing financial interests or person relationships that could have appeared to influence the work reported in this paper.

Acknowledgments

We sincerely thank the Editor Ling Chen and two anonymous reviewers for their insightful and constructive comments which improved the manuscript significantly. The broadband seismic data used in this study were provided by Data Management Center of China National Seismic Network at Institute of Geophysics, China Earthquake Administration (SEISDMC, doi: [10.11998/SeisDmc/SN](https://doi.org/10.11998/SeisDmc/SN)). The strong motion data were provided by Institute of Engineering Mechanics, China Earthquake Administration. The Sentinel-1 data were provided by the European Space Agency (ESA) data hub. The ALOS-2 data were provided by JAXA through the RA6 ALOS-2 project (ID: 3159). Some of the figures were made using the Generic Mapping Tools (Wessel and Smith, 1998). X. Zhang was supported by the Special Fund of the Institute of Geophysics, China Earthquake Administration (DQJB19B20) and National Natural Science Foundation of China (41804088). W. Feng was partly supported by Geological Processes and Natural Disasters around

the South China Sea (311020002), the Second Tibetan Plateau Scientific Expedition and Research Program (STEP) (2019QZKK0901), the Guangdong Basic and Applied Basic Research Foundation (2020A1515011078), and Guangdong Province Introduced Innovative R&D Team of Geological Processes and Natural Disasters around the South China Sea (2016ZT06N331). F. Yin was supported by the National Natural Science Foundation of China (41804094).

Appendix A. Supplementary data

Supplementary data to this article can be found online at <https://doi.org/10.1016/j.tecto.2021.229118>.

References

- Allen, C.R., Luo, Z., Qian, H., Wen, X., Zhou, H., Huang, W., 1991. Field study of a highly active fault zone: The Xianshuihe fault of southwestern China. *Geol. Soc. Am. Bull.* 103, 1178–1199.
- Avouac, J.-P., Meng, L., Wei, S., Wang, T., Ampuero, J.-P., 2015. Lower edge of locked Main Himalayan Thrust unzipped by the 2015 Gorkha earthquake. *Nat. Geosci.* 8, 708–711.
- Beroza, G.C., Zoback, M.D., 1993. Mechanism diversity of the Loma Prieta aftershocks and the mechanics of mainshock-aftershock interaction. *Science* 259, 210–213.
- Bletery, Q., Sladen, A., Delouis, B., Vallée, M., Nocquet, J.-M., Rolland, L., Jiang, J., 2014. A detailed source model for the M_W 9.0 Tohoku-Oki earthquake reconciling geodesy, seismology, and tsunami records. *J. Geophys. Res.* 119, 7636–7653.
- Boatwright, J., Thywissen, K., Seekins, L.C., 2001. Correlation of ground motion and intensity for the 17 January 1994 Northridge, California, earthquake. *Bull. Seismol. Soc. Am.* 91, 739–752.
- Cesca, S., Zhang, Y., Mouslopoulou, V., Wang, R., Saul, J., Savage, M., Heimann, S., Kufner, S.K., Oncken, O., Dahm, T., 2017. Complex rupture process of the M_w 7.8, 2016, Kaikoura earthquake, New Zealand, and its aftershock sequence. *Earth Planet. Sci. Lett.* 478, 110–120.
- Chen, K., Avouac, J.-P., Aati, S., Milliner, C., Zheng, F., Shi, C., 2020. Cascading and pulse-like ruptures during the 2019 Ridgecrest earthquakes in the Eastern California Shear Zone. *Nat. Commun.* 11, 22.
- Corbi, F., Funicello, F., Brizzi, S., Lallemand, S., Rosenau, M., 2017. Control of asperities size and spacing on seismic behavior of subduction megathrusts. *Geophys. Res. Lett.* 44, 8227–8235.
- Das, S., Henry, C., 2003. Spatial relation between main earthquake slip and its aftershock distribution. *Rev. Geophys.* 41, 1013.
- Donner, S., Ghods, A., Krüger, F., Rößler, D., Landgraf, A., Ballato, P., 2015. The Ahar-Varzeghan earthquake doublet (M_W 6.4 and 6.2) of 11 August 2012: Regional seismic moment tensors and a seismotectonic interpretation. *Bull. Seismol. Soc. Am.* 105, 791–807.
- Fang, L., Wu, J., Liu, J., Cheng, J., Jiang, C., Han, L., Wang, Y., Chen, K., Zhao, X., Wu, Z., 2015. Preliminary report on the 22 November 2014 M_W 6.1/ M_S 6.3 Kangding earthquake, western Sichuan, China. *Seismol. Res. Lett.* 86, 1603–1613.
- Fang, L., Wu, J., Su, J., Wang, M., Jiang, C., Fan, L., Wang, W., Wang, C., Tan, X., 2018. Relocation of mainshock and aftershock sequence of the M_S 7.0 Sichuan Jiuzhaigou earthquake. *Chin. Sci. Bull.* 63, 649–662.
- Farr, T.G., Rosen, P.A., Caro, E., Crippen, R., Duren, R., Hensley, S., Kobrick, M., Paller, M., Rodriguez, E., Roth, L., Seal, D., Shaffer, S., Shimada, J., Umland, J., Werner, M., Oskin, M., Burbank, D., Alsdorf, D., 2007. The Shuttle Radar Topography Mission. *Rev. Geophys.* 45, RG2004.
- Feng, W., Li, Z., Elliott, J.R., Fukushima, Y., Hoey, T., Singleton, A., Cook, R., Xu, Z., 2013. The 2011 M_W 6.8 Burma earthquake: fault constraints provided by multiple SAR techniques. *Geophys. J. Int.* 195, 650–660.
- Feng, W., Omari, K., Samsonov, S.V., 2016. An automated InSAR processing system: Potentials and challenges. In: *IEEE International Geoscience and Remote Sensing Symposium*, pp. 3209–3210.
- Feng, W., Samsonov, S., Qiu, Q., Wang, Y., Zhang, P., Li, T., Zheng, W., 2020. Orthogonal fault rupture and rapid postseismic deformation following 2019 Ridgecrest, California, earthquake sequence revealed from geodetic observations. *Geophys. Res. Lett.* 47 e2019GL086888.
- Galović, F., Zahradník, J., Plicka, V., Sokos, E., Evangelidis, C., Fountoulakis, I., Turhan, F., 2020. Complex rupture dynamics on an immature fault during the 2020 M_w 6.8 Elazığ earthquake, Turkey. *Communicat. Earth Environ.* 1, 40.
- Gan, W., Zhang, P., Shen, Z.-K., Niu, Z., Wang, M., Wan, Y., Zhou, D., Cheng, J., 2007. Present-day crustal motion within the Tibetan Plateau inferred from GPS measurements. *J. Geophys. Res.* 112, B08416.
- Graizer, V., 2006. Tilts in strong ground motion. *Bull. Seismol. Soc. Am.* 96, 2090–2102.
- Gusman, A.R., Murotani, S., Satake, K., Heidarzadeh, M., Gunawan, E., Watada, S., Schurr, B., 2015. Fault slip distribution of the 2014 Iquique, Chile, earthquake estimated from ocean-wide tsunami waveforms and GPS data. *Geophys. Res. Lett.* 42, 1053–1060.
- Harris, R.A., 2017. Large earthquakes and creeping faults. *Rev. Geophys.* 55, 169–198.
- Hartzell, S., Mendoza, C., Ramirez-Guzman, L., Zeng, Y., Mooney, W., 2013. Rupture history of the 2008 M_W 7.9 Wenchuan, China, earthquake: Evaluation of separate and joint inversions of geodetic, teleseismic, and strong-motion data. *Bull. Seismol. Soc. Am.* 103, 353–370.

- Jiang, G., Wen, Y., Liu, Y., Xu, X., Fang, L., Chen, G., Gong, M., Xu, C., 2015a. Joint analysis of the 2014 Kangding, southwest China, earthquake sequence with seismicity relocation and InSAR inversion. *Geophys. Res. Lett.* 42, 3273–3281.
- Jiang, G., Xu, X., Chen, G., Liu, Y., Fukahata, Y., Wang, H., Yu, G., Tan, X., Xu, C., 2015b. Geodetic imaging of potential seismogenic asperities on the Xianshuihe-Anninghe-Zemuhe fault system, southwest China, with a new 3-D viscoelastic interseismic coupling model. *J. Geophys. Res.* 120, 1855–1873.
- Kim, A., Dreger, D.S., Taira, T.a., Nadeau, R.M., 2016. Changes in repeating earthquake slip behavior following the 2004 Parkfield main shock from waveform empirical Green's functions finite-source inversion. *J. Geophys. Res.* 121, 1910–1926.
- King, G.C.P., Stein, R.S., Lin, J., 1994. Static stress changes and the triggering of earthquakes. *Bull. Seismol. Soc. Am.* 84, 935–953.
- Koper, K.D., Pankow, K.L., Pechmann, J.C., Hale, J.M., Burlacu, R., Yeck, W.L., Benz, H. M., Herrmann, R.B., Trugman, D.T., Shearer, P.M., 2018. Afterslip enhanced aftershock activity during the 2017 earthquake sequence near Sulphur Peak, Idaho. *Geophys. Res. Lett.* 45, 5352–5361.
- Li, L., Wang, B., Peng, Z., Li, D., 2019. Dynamic triggering of microseismicity in Southwest China following the 2004 Sumatra and 2012 Indian Ocean earthquakes. *J. Asian Earth Sci.* 176, 129–140.
- Mendoza, C., Hartzell, S.H., 1988. Aftershock patterns and main shock faulting. *Bull. Seismol. Soc. Am.* 78, 1438–1449.
- Ozawa, S., Ando, R., 2021. Mainshock and aftershock sequence simulation in geometrically complex fault zones. *J. Geophys. Res.* 126 e2020JB020865.
- Perfettini, H., Frank, W.B., Marsan, D., Bouchon, M., 2018. A Model of aftershock migration driven by afterslip. *Geophys. Res. Lett.* 45, 2283–2293.
- Ross, Z.E., Rollins, C., Cochran, E.S., Hauksson, E., Avouac, J.-P., Ben-Zion, Y., 2017. Aftershocks driven by afterslip and fluid pressure sweeping through a fault-fracture mesh. *Geophys. Res. Lett.* 44, 8260–8267.
- Sandwell, D., Mellors, R., Tong, X., Wei, M., Wessel, P., 2011. Open radar interferometry software for mapping surface deformation. *EOS Trans. Am. Geophys. Union* 92, 234.
- Shan, B., Xiong, X., Wang, R., Zheng, Y., Yang, S., 2013. Coulomb stress evolution along Xianshuihe-Xiaojiang Fault System since 1713 and its interaction with Wenchuan earthquake, May 12, 2008. *Earth Planet. Sci. Lett.* 377–378, 199–210.
- Shapiro, S.A., Huenges, E., Borm, G., 1997. Estimating the crust permeability from fluid-injection-induced seismic emission at the KTB site. *Geophys. J. Int.* 131, F15–F18.
- Shcherbakov, R., Turcotte, D.L., 2004. A modified form of Båth's law. *Bull. Seismol. Soc. Am.* 94, 1968–1975.
- Shelly, D.R., Hill, D.P., Massin, F., Farrell, J., Smith, R.B., Taira, T.a., 2013. A fluid-driven earthquake swarm on the margin of the Yellowstone caldera. *J. Geophys. Res.* 118, 4872–4886.
- Shelly, D.R., Ellsworth, W.L., Hill, D.P., 2016. Fluid-faulting evolution in high definition: Connecting fault structure and frequency-magnitude variations during the 2014 Long Valley Caldera, California, earthquake swarm. *J. Geophys. Res.* 121, 1776–1795.
- Simons, M., Fialko, Y., Rivera, L., 2002. Coseismic deformation from the 1999 M_W 7.1 Hector Mine, California, earthquake as inferred from InSAR and GPS observations. *Bull. Seismol. Soc. Am.* 92, 1390–1402.
- van der Elst, N.J., Brodsky, E.E., 2010. Connecting near-field and far-field earthquake triggering to dynamic strain. *J. Geophys. Res.* 115, B07311.
- Waldhauser, F., Ellsworth, W.L., 2000. A double-difference earthquake location algorithm: Method and application to the Northern Hayward fault, California. *Bull. Seismol. Soc. Am.* 90, 1353–1368.
- Wallace, L.M., Kaneko, Y., Hreinsdóttir, S., Hamling, I., Peng, Z., Bartlow, N., D'Anastasio, E., Fry, B., 2017. Large-scale dynamic triggering of shallow slow slip enhanced by overlying sedimentary wedge. *Nat. Geosci.* 10, 765–770.
- Wang, R., 1999. A simple orthonormalization method for stable and efficient computation of Green's functions. *Bull. Seismol. Soc. Am.* 89, 733–741.
- Wang, R., Martin, F.L., Roth, F., 2003. Computation of deformation induced by earthquakes in a multi-layered elastic crust—FORTRAN programs EDGRN/EDCMP. *Comput. Geosci.* 29, 195–207.
- Wang, R., Lorenzo-Martín, F., Roth, F., 2006. PSGRN/PSCMP—a new code for calculating co- and post-seismic deformation, geoid and gravity changes based on the viscoelastic-gravitational dislocation theory. *Comput. Geosci.* 32, 527–541.
- Wang, R., Parolai, S., Ge, M., Jin, M., Walter, T.R., Zschau, J., 2013. The 2011 M_w 9.0 Tohoku earthquake: Comparison of GPS and strong-motion data. *Bull. Seismol. Soc. Am.* 103, 1336–1347.
- Ward, S.N., Barrientos, S.E., 1986. An inversion for slip distribution and fault shape from geodetic observations of the 1983, Borah Peak, Idaho. *Earthquake. J. Geophys. Res.* 91, 4909–4919.
- Warren-Smith, E., Chamberlain, C.J., Lamb, S., Townend, J., 2017. High-precision analysis of an aftershock sequence using matched-filter detection: The 4 May 2015 M_L 6 Wanaka earthquake, southern Alps, New Zealand. *Seismol. Res. Lett.* 88, 1065–1077.
- Wells, D.L., Coppersmith, K.J., 1994. New empirical relationships among magnitude, rupture length, rupture width, rupture area, and surface displacement. *Bull. Seismol. Soc. Am.* 84, 974–1002.
- Wen, X.-Z., Ma, S.-L., Xu, X.-W., He, Y.-N., 2008. Historical pattern and behavior of earthquake ruptures along the eastern boundary of the Sichuan-Yunnan faulted-block, southwestern China. *Phys. Earth Planet. Inter.* 168, 16–36.
- Wessel, P., Smith, W.H.F., 1998. New, improved version of generic mapping tools released. *EOS Trans. Am. Geophys. Union* 79, 579.
- Wetzler, N., Lay, T., Brodsky, E.E., Kanamori, H., 2018. Systematic deficiency of aftershocks in areas of high coseismic slip for large subduction zone earthquakes. *Sci. Adv.* 4 eaao3225.
- Yabe, S., Ide, S., 2018. Why do aftershocks occur within the rupture area of a large earthquake? *Geophys. Res. Lett.* 45, 4780–4787.
- Yi, G.-X., Wen, X.-Z., Su, Y.-J., 2008. Study on the potential strong-earthquake risk for the eastern boundary of the Sichuan-Yunnan active faulted-block. *Chin. J. Geophys.* 51, 1719–1725.
- Yi, G.-X., Long, F., Wen, X.-Z., Liang, M.-J., Wang, S.-W., 2015. Seismogenic structure of the $M_6.3$ Kangding earthquake sequence on 22 Nov. 2014, Southwestern China. *Chin. J. Geophys.* 58, 1205–1219.
- Yue, H., Lay, T., Rivera, L., An, C., Vigny, C., Tong, X., Báez Soto, J.C., 2014. Localized fault slip to the trench in the 2010 Maule, Chile $M_w = 8.8$ earthquake from joint inversion of high-rate GPS, teleseismic body waves, InSAR, campaign GPS, and tsunami observations. *J. Geophys. Res.* 119, 7786–7804.
- Yue, H., Ross, Z.E., Liang, C., Michel, S., Fattahi, H., Fielding, E., Moore, A., Liu, Z., Jia, B., 2017. The 2016 Kumamoto $M_w = 7.0$ earthquake: A significant event in a fault-volcano system. *J. Geophys. Res.* 122, 9166–9183.
- Zhang, Y., Feng, W., Chen, Y., Xu, L., Li, Z., Forrest, D., 2012. The 2009 L'Aquila M_W 6.3 earthquake: a new technique to locate the hypocentre in the joint inversion of earthquake rupture process. *Geophys. J. Int.* 191, 1417–1426.
- Zhang, X., Feng, W., Du, H., Li, L., Wang, S., Yi, L., Wang, Y., 2020a. The 2018 M_W 7.5 Papua New Guinea earthquake: A dissipative and cascading rupture process. *Geophys. Res. Lett.* 47 e2020GL089271.
- Zhang, X., Xu, L.S., Luo, J., Feng, W., Du, H.L., Li, L., Yi, L., Zheng, C., Li, C.L., 2020b. Source characteristics of the 2017 M_S 6.6 (M_W 6.3) Jinghe earthquake in the northeastern Tien Shan. *Seismol. Res. Lett.* 91, 745–757.